Deep Learning with Synthetic Hyperspectral Images for Improved Soil Detection in Multispectral Imagery

Yan Lu
Old Dominion University
Norfolk, VA, USA
yxxlu003@odu.edu

Daniel Perez
Old Dominion University
Norfolk, VA, USA
dpere013@odu.edu

Minh Dao
Applied Research LLC
Rockville, Maryland, USA
ducminh174@gmail.com

Chiman Kwan
Applied Researech LLC
Rockville, Maryland, USA
chiman.kwan@arllc.net

Jiang Li
Old Dominion University
Norfolk, VA, USA
jli@odu.edu

***Abstract*—Remote sensing images play a critical role in natural disaster prevention and damage estimation. With the fast advances in hyperspectral sensors, the hyperspectral imaging also known as imaging spectrometry is becoming a relatively recent trend. Hyperspectral images are expected to be more effective in object detection, environmental monitoring, urban growth monitoring, and damage assessment. In this paper, we present a 4 layers deep convolutional neural network (CNN) model for soil detection by using the combination of 80 synthetic hyperspectral bands and its original 8 multispectral bands which are collected by the WorldView-2 satellite. Our experiment result shows that by using the combined 80 synthetic hyperspectral bands and the original 8 multispectral bands, the area under the curve (AUC) scores of our CNN model for soil detection on the three testing images has been improved by 7.42% in average from 76.26% to 83.48%, as compared to the result by using the 8 multispectral bands alone. We also applied the CNN model onto a set of high-resolution data which is created by pan-sharpening the original multispectral bands and its synthetic hyperspectral bands, which quadrupled the spatial resolution of the combined synthetic hyperspectral bands. With the increased spatial resolution of the combined synthetic hyperspectral bands, the average AUC scores of our CNN model was furtherly improved by 10.02% from 81.44% to 91.47%. This significant improvement indicates that by using the pan-sharpened synthetic hyperspectral bands, the performance of CNN model for soil detection has been greatly improved, the synthetic hyperspectral bands with increased spatial resolution is a great alternative in improving the performance of object detection and classification in remote sensing applications.**

Keywords— Soil Detection, Deep Learning, Convolutional Neural Network, Remote Sensing, Synthetic Hyperspectral Images, Multispectral Satellite Images, EMAP, Imbalanced Data, Post-Processing

I. INTRODUCTION

Remote sensing images play a critical role in natural disaster prevention and damage estimation, such as landslide detection and flood damage estimation. Multispectral images, which usually refers to images with 3 to 10 bands, have been widely and regularly used in the remote sensing area since the 1970s. With the fast advances of hyperspectral sensors, the hyperspectral imagery also known as imaging spectrometry, which contains many more bands with much narrower bandwidth (10-20 nm) than multispectral bands are expected to be more effective in target identification [1][2], land cover classification [3], anomalous materials and objects detection [4][5]. NASA is planning a mission that will have a hyperspectral imager [6][7] covering the whole Earth for vegetation monitoring.

Nonetheless, hyperspectral imagery data might not always be available. As an alternative, spectral dimensionality expanding methods [8] can be used to create synthetic hyperspectral bands by applying it to the original multispectral bands. The synthetic hyperspectral bands might not have the same physical meanings as the real hyperspectral bands do, however, it is generally expected and accepted that the synthetic hyperspectral bands, which hold the correlations with the spatial characteristics of the objects along with the spectral information contained in the original images, are highly likely to achieve better object detection and classification results than the regular multispectral bands [9].

Deep learning networks have been widely used in image processing and classification tasks in recent years [10] [11] [12]. It has achieved a lot of remarkable performances in a wide range of computer vision and image classification tasks [13] [14] [15]. In our previous research [16], a deep 4-layer convolutional neural network (CNN) was proposed for soil detection by using the WorldView-2 8-band multispectral pan-sharpened images. Our results showed that the deep CNN model is very effective in the soil detection task.

In this paper, we conduct further investigations on our previously proposed CNN model by using 80 synthetic hyperspectral bands generated by the spectral dimensionality expanding methods [8] combined with the original 8 multispectral bands for soil detection. Our experimental results show that with the additional information contented in the synthetic hyperspectral bands, the soil detection performance of our CNN model is significantly improved than that using the 8 multispectral bands alone.

The remainder of this paper is organized as follows. Section II introduces the hyperspectral synthetic method, data

This research was supported by DARPA under contract #140D6318C0043. The views, opinions and/or findings expressed are those of the author and should not be interpreted as representing the official views or policies of the Department of Defense or the U.S. Government.

978-1-5386-7693-6/18/$31.00 ©2018 IEEE

preparation procedure, the CNN model, imbalanced learning and post-processing techniques used for soil detection. Section III summarizes soil detection training and testing results. Section IV shows the effect of post-processing and Section V concludes this paper.

II. Methodology

A. Synthetic hyperspectral bands

The satellite images used in this study were captured by the Worldview-2 (WV-2) satellite, which contain 8 multispectral image channels. The first step is to use both spectral and spatial information of the 8 channels to generate a newly expanded image with high dimensional synthetic bands.

In this step, we used Extended Multi-Attribute Profile (EMAPs) [8] to generate 80 synthetic hyperspectral bands as shown in Fig. 1. EMAP is an extended idea of attribute profile (AP), a method that has recently been presented as an efficient tool for spectral-spatial analysis of remote sensing images. APs provide a multi-level characterization of an image obtained by applying a sequence of morphological attribute filters to model different kinds of structural information on a single-band (or grayscale) image. These attribute filters can be morphological operators (so-called features) such as thinning or thickening operators that process an image by merging its connected pixels. APs using different types of attribute features on different threshold levels can be stacked together, generating EMAPs.

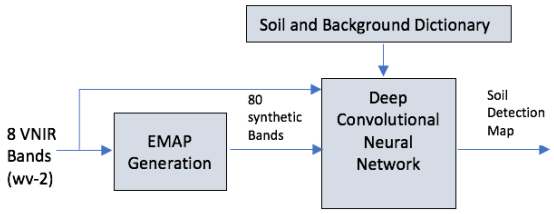

Fig. 1. EMAP synthetic hyperspectral bands generation and overall soil detection framework.

B. Training data

Soil class samples are collected in the red oval areas as shown in Fig. 2. Other than the soil class, there are 13 other classes of land cover types including cars, white trucks, black trucks, gray buildings, strip-shape-buildings, roads, runways, checkerboard shaped land, land near runways, land near soil, general trees, trees near soil and parking lots. All classes samples are collected in the areas as shown in Fig. 3. The masks of these 14 classes are created manually using Matlab by visual inspection.

Fig. 2. Soil samples in WV-2.

Besides the original 8-channel multispectral bands and the 80-channel synthetic hyperspectral bands in the original resolution, we applied a pan-sharpening technique [17] to the 8-channel multispectral data and the 80-channel synthetic hyperspectral data in the original resolution (low-resolution). We obtained another training dataset in quadrupled resolution (high-resolution) as well. The pan-sharpening of multispectral images was carried out by Dao *et al.* [17] by using the Gram-Schmidt Adaptive (GSA) technique [18].

To train the CNN model, we extracted patches for different classes using the masks as shown in Fig. 3. Patches are extracted with patch sizes of 7x7x8 and 7x7x88 from the 8-channel original multispectral data and the combined synthetic 88-channel hyperspectral data in both low-resolution and high-resolution cases. Details of the extracted training patches for different classes are shown in Table I.

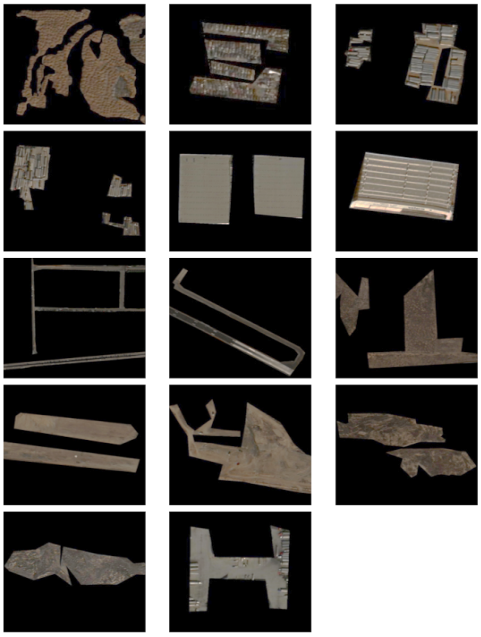

Fig. 3. All 14 classes of training samples.

TABLE I. Description of 14 classes

Class Name	Class ID	Number of Patches 7x7x8 & Patches 7x7x88 in high resolution	Number of Patches 7x7x8 & Patches 7x7x88 in low resolution
Soil	1	89,520	5,537
Car	2	68,118	4,286
Truck-White	3	70,599	6,341
Truck-Black	4	78,003	4,911
Building-Gray	5	461,257	28,769
Building-Strip	6	71,051	4,474
Road	7	635,539	39,404
Runway	8	588,135	36,826
Land-Checkerboard	9	850,743	53,226
Land-Runway	10	1,393,342	87,137
Land-Near-Soil	11	213,489	18,040
Tree-Near-Soil	12	492,081	30,038
Tree-General	13	187,812	17,169
Parking-Lot	14	141,556	13,343

C. Testing data

By manually screening through 12 sets of WV-2 Pan-VNIR images, three images dated 03/19/2010, 10/11/2010 and 12/02/2010 were selected for testing. The contour of the masks of ground truth of soil area in the three images were developed manually as shown in Fig. 4.

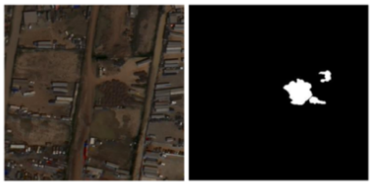

(a) Testing image 1 captured on 03/19/2010

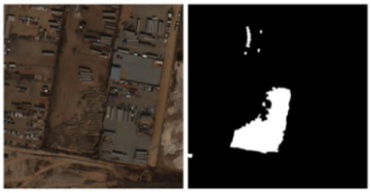

(b) Testing image captured on 10/11/2010

(c) Testing image captured on 12/02/2010

Fig. 4. Testing images and ground truth masks.

D. CNN structure

We used the same structure for the CNN model as in our previous work [16], except the filter size in the first convolution layer changed accordingly to be consistent with the input patch sizes. The CNN Model has three convolutional layers with various filter sizes and a fully connected layer with 100 hidden units, as shown in Fig. 5.

Each convolutional layer utilizes the Rectified Linear Unit (ReLu) as activation function, the last fully connected layer uses the SoftMax function for classification. We add dropout layer for each convolutional layer with a dropout rate of '0.1' to mitigate overfitting [19].

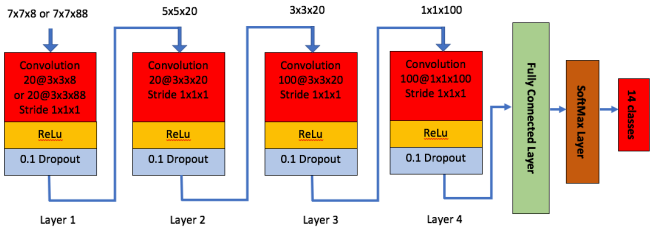

Fig. 5. The CNN model structure.

E. Imbalance learning

We collected 14 classes in total for training, however, the goal of this project is to detect the soil class. Accurately identifying the other class types is not our major concern. Furthermore, the training dataset is highly unbalanced as shown in Table I, of which some classes have significant more samples than others. Traditional imbalance learning methods include down-sampling majority classes or up-sampling minority classes to balance the data. In our study, to solve this imbalance learning problem, we randomly sample all classes to the smallest patch number among all of the classes (68,118 in high resolution and 4,286 in low resolution) before training. In the following training phase, we train the CNN model to classify all the 14 classes. In testing, we convert the 14-classes problem to 2-classes problem by using the following conversion formula,

$$P'_{Soil} = \frac{P_{Soil}}{P_{Soil} + \max(P_{Non-Soil})}$$

$$P'_{Non-Soil} = \frac{\max(P_{Non-Soil})}{P_{Soil} + max\,(P_{Non-Soil})}$$

where P_{Soil} and $P_{Non-Soil}$ are the probabilities of the soil and all non-soil classes predicted by the CNN model, while P'_{Soil} and $P'_{Non-Soil}$ are the converted 2-classes probabilities of soil class and non-soil class.

F. Post-processing

After we obtained soil probability map for a testing image, we applied the morphological closing operation filter to it to enforce group sparsity across neighbor pixels. This process can reduce false positive and connect isolated soil regions [19]. A low-pass filter was then applied to smooth out the soil map. We computed ROC curves and AUC scores as the performance metrics for comparing different methods.

III. Experimental Results

A. Experimental setup

In this stage, we train the corresponding CNN models in accordance with the combined 88-channel hyperspectral and 8-channel multispectral data in both high-resolution and low-resolution scenario. We train the CNNs with a batch size of 64, the training is stopped when the CNNs are starting get converged at around 150 epochs of training. Then we save the corresponding models for the different testing scenario.

B. Testing results without post-processing

After we got the trained CNN models for soil detection task for both the high-resolution and low-resolution data, we apply the trained model on the three testing images to detect soil. Our results show that:

1) In all the three testing images, by using the combined synthetic 88-channel hyperspectral data, the AUC scores for both high-resolution and low-resolution are all improved. The improvement is ranged from 0.61% to 28.74% in different testing scenarios. For the three different images, the overall AUC has been improved, on average, 9.02% for high-resolution data, and 7.42% for low-resolution data.

(2) From our testing results, the combined 88-channel hyperspectral data achieved the largest boost for soil detection on the testing image dated March 9th, 2010 as compared to the 8-channel multispectral data. The AUC is significantly improved by 28.74% for high-resolution data and 9.72% for low-resolution data in this testing image.

The detailed results by using the synthetic 88-channel hyperspectral data and the 8-channel multispectral data in the three testing areas are shown in the subsequent subsections.

1) Results on the testing area dated 3/19/2010

Fig. 6 shows the testing results obtained on the testing image taken on 03/19/2010. For this testing area, the AUC scores of our CNN soil detection model using 88-channel hyperspectral data and 8-channel multispectral data are 96.19% and 67.45% in high resolution, and 84.84% and 75.12% in low resolution, respectively. Using the synthetic hyperspectral data, it significantly improved the soil detection performances.

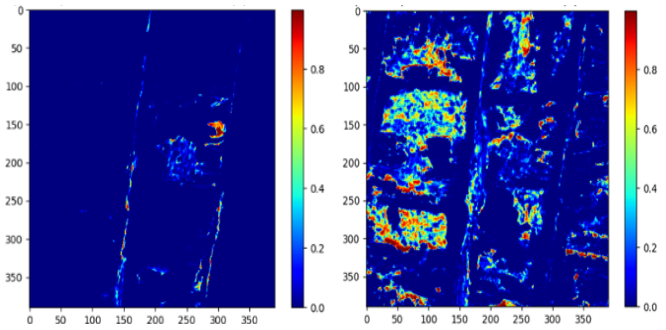

(a) High-resolution results for testing area dated 3/19/2010. Left: Soil prediction map by 88-band data. Right: Soil prediction map by 8-band data.

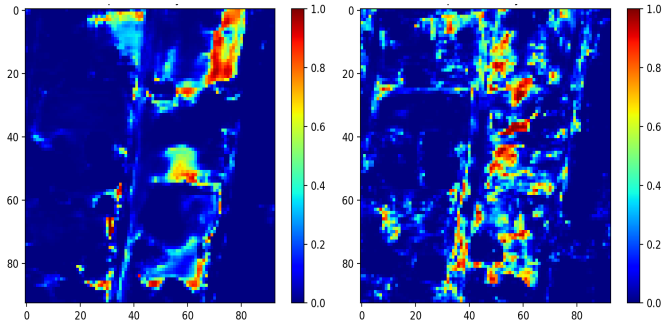

(b) Low-resolution results for testing area dated 3/19/2010. Left: Soil prediction map by 88-band data. Right: Soil prediction map by 8-band data.

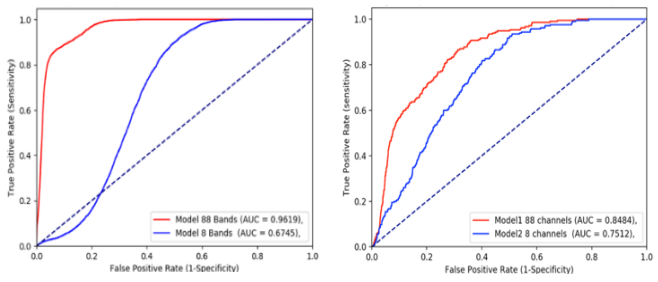

(c) Left: ROC curves for the results in Fig. 6a). Right: ROC curves for the results in Fig. 6b).

Fig. 6. Soil detection results for the testing image dated 3/19/2010.

2) Results on the testing area dated 10/11/2010

Fig. 7 shows the testing results obtained on the testing image taken on 10/11/2010. For this testing area, the AUC scores of our CNN soil detection model using 88-channel hyperspectral data and 8-channel multispectral data are 86.54% and 85.82% in high resolution, and 78.57% and 77.15% in low resolution, respectively. All results are comparable for this testing area.

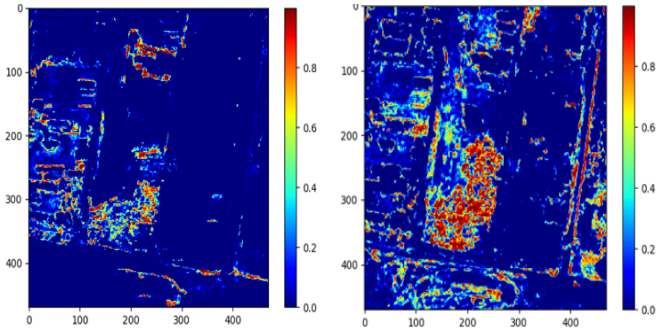

(a) High-resolution results for testing area dated 10/11/2010. Left: Soil prediction map by 88-band data. Right: Soil prediction map by 8-band data.

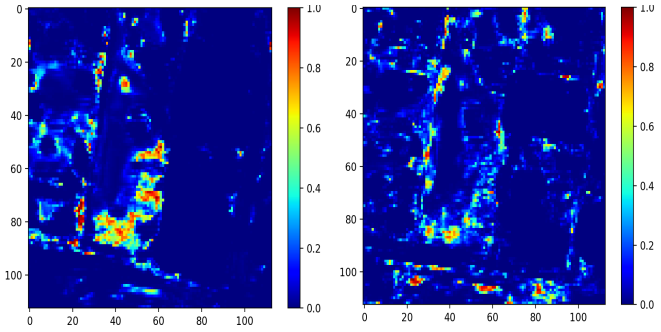

(b) Low-resolution results for testing area dated 10/11/2010. Left: Soil prediction map by 88-band data. Right: Soil prediction map by 8-band data.

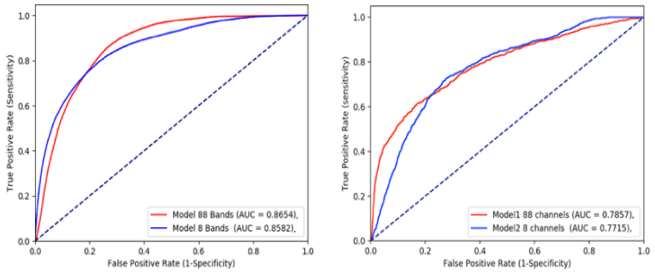

(c) Left: ROC curves for the results in Fig. 7a). Right: ROC curves for the results in Fig. 7b).

Fig. 7. Soil detection results for the testing area dated 10/11/2010.

3) Results on the testing area dated 12/2/2010

Fig. 8 shows the results obtained on the testing image taken on 12/02/2010. For this testing area, the AUC scores of our CNN soil detection model using 88-channel hyperspectral data and 8-channel multispectral data are 91.67% and 91.06% in high

resolution, and 87.03% and 75.51% in low resolution, respectively. The results for high-resolution data are comparable. The soil detection result is significantly improved by using the combined 88-channel hyperspectral data over the 8-channel multispectral data for low-resolution data.

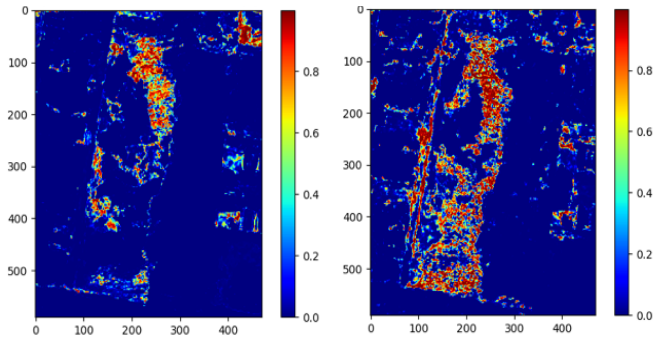

(a) High-resolution results for testing area dated 12/2/2010. Left: Soil prediction map by 88-band data. Right: Soil prediction map by 8-band data.

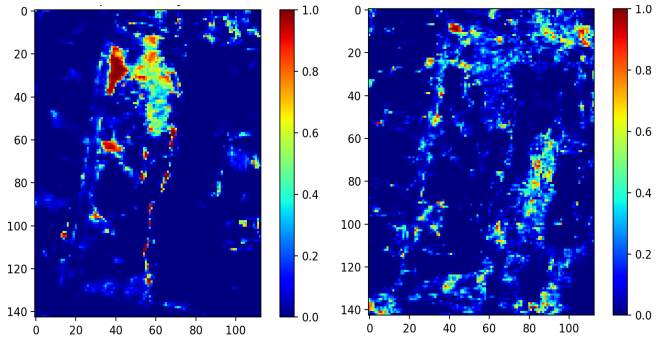

(b) Low-resolution results for testing area dated 12/2/2010. Left: Soil prediction map by 88-band data. Right: Soil prediction map by 8-band data.

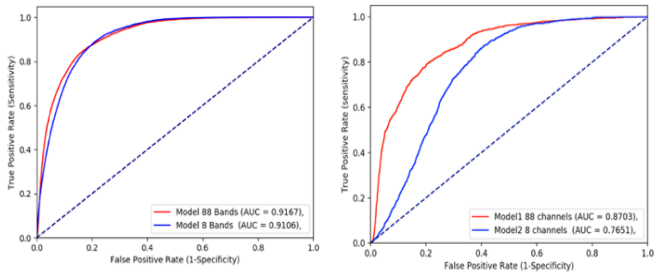

(c) Left: ROC curves for the results in Fig. 8a). Right: ROC curves for the results in Fig. 8b).

Fig. 8. Soil detection results for the testing area dated 12/2/2010.

C. *Effect of post-processing*

The soil detection results in the previous subsection demonstrated the benefits of using the 88-channel hyperspectral data, the soil detection performance of our CNN model has been significantly improved. In this subsection, we further applied post-processing with morphological filters to the results of 88-channels hyperspectral data. Our experiment results show that by post-processing, the results can be improved further.

1) Post-processing effect on the testing area dated 3/19/2010

Fig. 9a) shows that the detection results of soil prediction map before and after the post-processing using 88-channel hyperspectral data in high resolution, and Fig. 9b) shows the detection results of soil prediction map before and after the post-processing using 88-channel hyperspectral in low-resolution. Figs. 9c) shows the ROC curves before and after the application of the post-processing in both the high resolution and low-resolution cases. The AUC scores were improved by 1.52% in high-resolution and 2.28% in low-resolution, respectively.

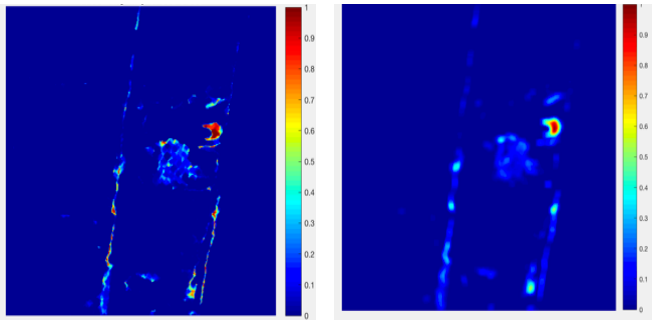

(a) Left: Probability map of soil before post-processing 88-band in high resolution. Right: Probability map of soil after post-processing 88-band in high resolution.

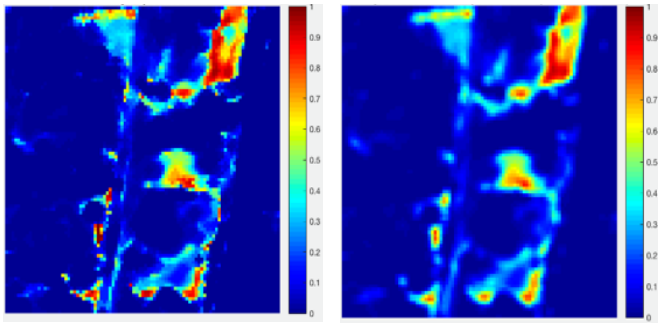

(b) Left: Probability map of soil before post-processing 88-band in low resolution. Right: Probability map of soil after post-processing 88-band in low resolution.

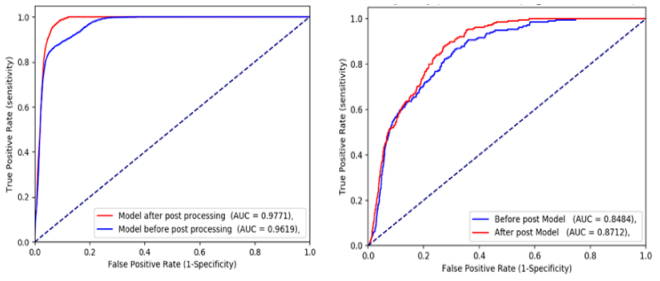

(c) Left: ROC curves before and after post processing in high resolution. Right: ROC curves before and after post processing in low resolution.

Fig. 9. Post-processing results for testing image dated 3/19/2010.

2) Post-processing effect on the testing area dated 10/11/2010

Fig. 10a) shows detection results before and after the post processing step on the soil prediction map produced by using 88-channel hyperspectral data in high resolution, and Fig. 10b) shows the corresponding results for the low-resolution case. Figs. 10c) shows the ROC curves before and after the application of the post-processing step in both the high-resolution and low-resolution cases. The AUC scores were improved by 5.95% in high-resolution and 4.63% in low-resolution, respectively.

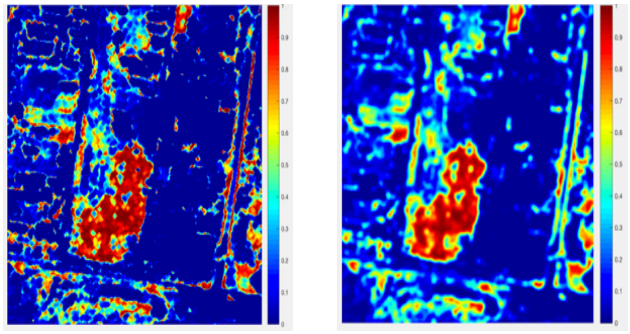

(a) Left: Probability map of soil before post-processing. Right: Probability map of soil after post-processing in high resolution.

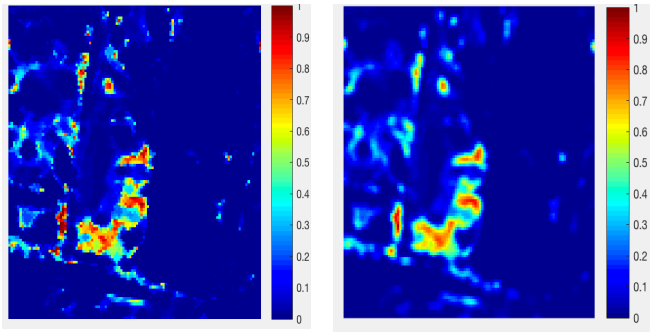

(b) Left: Probability map of soil before post-processing. Right: Probability map of soil after post-processing in low resolution.

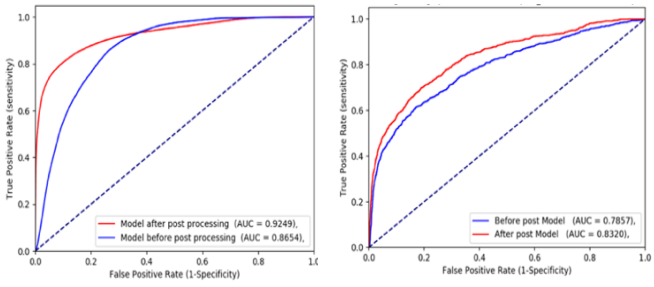

(c) Left: ROC curves before and after post-processing in high resolution. Right: ROC curves before and after post-processing in low resolution.

Fig. 10. Post-processing results for testing image dated 10/11/2010.

3) Post-processing effect on the testing area dated 12/2/2010

Fig. 11a) shows detection results before and after the post-processing step on the soil prediction map produced by using 88-channel hyperspectral data in high resolution, and Fig. 11b) shows the corresponding results for the low-resolution case. Figs. 11c) shows the ROC curves before and after the application of the post-processing step in both the high resolution and low-resolution cases. The AUC scores were improved by 2.48% in high-resolution and 1.64% in low-resolution, respectively.

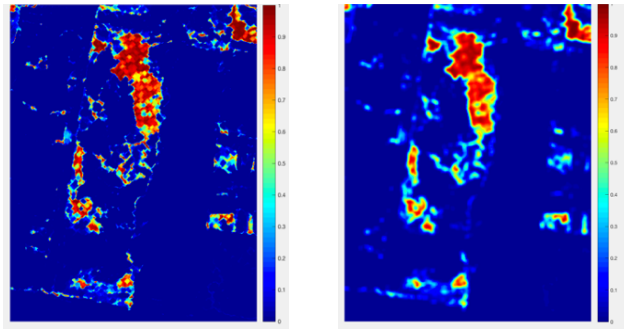

(a) Left: Probability map of soil before post-processing. Right: Probability map of soil after post-processing in high resolution.

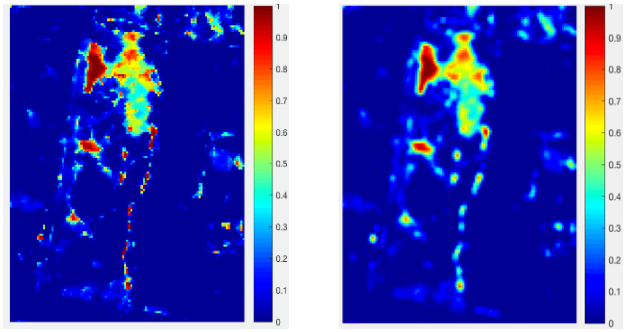

(b) Left: Probability map of soil before post-processing. Right: Probability map of soil after post-processing in low resolution.

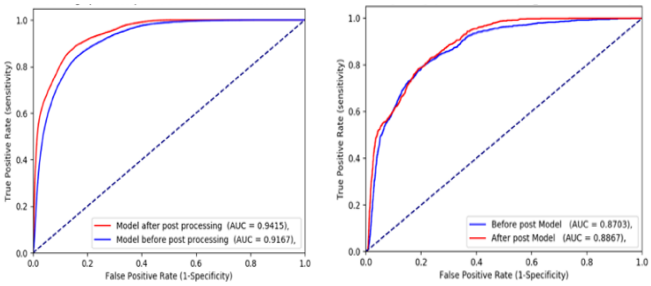

(c) Left: ROC curves before and after post-processing in high resolution. Right: ROC curves before and after post-processing in low resolution.

Fig. 11. Post-Processing results for testing image dated 10/11/2010.

TABLE II. AUC SCORES OF CNN MODELS ON TESTING AREAS

Soil Detection CNN Models	AUC Scores		
	Testing area 3/19/2010	*Testing area 10/11/2010*	*Testing area 12/2/2010*
8_High_Resolution	0.6745	0.8582	0.9106
88_High_Resolution	0.9619	0.8654	0.9167
Improvement Before Post Processing	**0.2874**	**0.0072**	**0.0061**
Improvement After Post Processing	**0.3026**	**0.0667**	**0.0309**
8_Low_Resolution	0.7512	0.7715	0.7651
88_Low_Resolution	0.8484	0.7857	0.8703
Improvement Before Post Processing	**0.0972**	**0.0142**	**0.1112**
Improvement After Post Processing	**0.1272**	**0.0605**	**0.1276**

Table II summarizes all testing results in Section V. It is observed that the CNN model achieved significantly better soil detection performances by using the 88-channel synthetic hyperspectral data for both the high-resolution and low-resolution cases. The pan-sharpened high-resolution data have a 0.5m spatial resolution while the low-resolution data have a 2m spatial resolution. The detection performance also benefited from the high-resolution images.

IV. CONCLUSION

We implemented a CNN model for soil detection in remote sensing images in this paper. The detection performance has been significantly improved by using 88-channel synthetic hyperspectral bands generated by the EMAP method. We also demonstrated that pan-sharpening and morphological post-processing can further improve the soil detection performance.

These results indicated that even though the synthetic hyperspectral bands may not have the same physical meanings as the real hyperspectral bands, they hold the correlations with the spatial characteristics of the objects. Along with the spectral information in the original bands, the synthetic hyperspectral data with increased spatial resolution is a good alternative for improving object detection and classification in remote sensing applications when real hyperspectral data is not available.

For the future work, we will investigate furtherly if there is a subset of the synthetic hyperspectral bands which highly correlated to the soil class and more efficient in detecting the soil class by using non-linear dimension deduction methods such as principle component analysis or deep autoencoder, by deducting the dimensions of the bands, it will highly likely accelerate the model training and expedite the convergence, and potentially improve the detection accuracy and increase the robustness of the CNN model.

REFERENCES

[1] Y. Chen, et al, "Hyperspectral image classification using dictionary-based sparse representation," IEEE Transactions on Geoscience and Remote Sensing 49 (10), 3973-3985.

[2] C. Kwan, B. Ayhan, G. Chen, C. Chang, J. Wang, and B. Ji, "A Novel Approach for Spectral Unmixing, Classification, and Concentration Estimation of Chemical and Biological Agents," IEEE Trans. Geoscience and Remote Sensing, vol. 44, no. 2, pp. 409-419, February 2006.

[3] B. Ayhan and C. Kwan, "Application of Deep Belief Network to Land Classification Using Hyperspectral Images," 14th International Symposium on Neural Networks, pp. 269-276, Hokkaido, Japan, June 2017.

[4] S. Li, W. Wang, H. Qi, B. Ayhan, C. Kwan, and S. Vance, "Low-rank Tensor Decomposition based Anomaly Detection for Hyperspectral Imagery," IEEE International Conference on Image Processing (ICIP), pp. 4525 – 4529, Quebec City, Canada, September 27-30, 2015.

[5] J. Zhou, C. Kwan, and B. Ayhan, "Hybrid In-Scene Atmospheric Compensation (H-ISAC) of Hyperspectral Images for High Performance Target Detection," International Symposium on Spectral Sensing Research, Missouri, July 2010.

[6] J. Zhou, H. Chen, B. Ayhan, and C. Kwan, "A High Performance Algorithm to Improve the Spatial Resolution of HyspIRI Images," NASA HyspIRI Science and Applications Workshop, Washington DC, Oct., 2012.

[7] C. Kwan, J. Yin, J. Zhou, H. Chen, and B. Ayhan "Fast Parallel Processing Tools for Future HyspIRI Data Processing," NASA HyspIRI Science Symposium, Greenbelt, Maryland, April 2013.

[8] S. Bernabé, P. R. Marpu, A. Plaza, and J. A. Benediktsson, "Spectral unmixing of multispectral satellite images with dimensionality expansion using morphological profiles," in Proc. SPIE Satell. Data Compression, Commun., Process., San Diego, CA, USA, 2012, vol. 8514, p. 85140Z.

[9] A.Davari, "GMM-Based Synthetic Samples for Classification of Hyperspectral Images with Limited Training Data," IEEE Geoscience and Remote Sensing Letters (Volume: 15, Issue: 6, June 2018).

[10] F.Li, G.Zhang, W.Wang, R.Xu, T.Schnell, J.Wen, F.McKenzie, J.Li, "Deep Models for Engagement Assessment With Scarce Label Information," IEEE Transactions on Human-Machine Systems, July 2017.

[11] D.Banerjee, K.Islam, G.Mei, L.Xiao, G.Zhang, R.Xu, S.Ji, J.Li, "A Deep Transfer Learning Approach for Improved Post-Traumatic Stress Disorder Diagnosis," IEEE International Conference on Data Mining (ICDM), November 2017.

[12] R.Li, W.Zhang, H.Suk, L.Wang, J.Li, D.Shen, S.Ji, "Deep learning based imaging data completion for improved brain disease diagnosis," Medical Image Computing and Computer-Assisted Intervention–MICCAI, pp305-312, January, 2014

[13] D.Ibanez, J. Li, Y. Shen, J.Dayanghirang, S.Wang, Z.Zheng, " Deep Learning for Pulmonary Nodule CT Image Retrieval—An Online Assistance System for Novice Radiologists," Data Mining Workshops (ICDMW), 2017 IEEE International Conference, 1112-1121.

[14] D. Perez, K. Islam, V. Hill, B. Schaeffer, R. Zimmerman, and J. Li, "Deepcoast: Quantifying seagrass distribution in coastal water through deep capsule networks," Chinese Conference on Pattern Recognitionand Computer Vision. Sun-Yat Sen University, 2018.

[15] K. Islam, D. Perez, V. Hill, B. Schaeffer, R. Zimmerman, and J. Li, "Seagrass detection in coastal water through deep capsule networks," Chinese Conference on Pattern Recognition and Computer Vision, Sun-Yat Sen University, 2018.

[16] D.Perez, D.Banerjee, C.Kwan, M.Dao, Y.Shen, K.Koperski, G.Marchisio, J.Li, "Deep Learning for Effective Detection of Excavated Soil Related to Illegal Tunnel Activities," IEEE Ubiquitous Computing Electronics and Mobile Communication Conference, p 626-632, 2017.

[17] M. Dao, C. Kwan, K. Koperski, and G. Marchisio, "A Joint Sparsity Approach to Tunnel Activity Monitoring Using High Resolution Satellite Images," IEEE Ubiquitous Computing, Electronics & Mobile Communication Conference, p 322-328, 2017.

[18] B.Aiazzi, S.Baronti, M, Selva. "Improving component substitution pansharpening through multivariate regression of ms+pan data," IEEE Transactions on Geoscience and Remote Sensing, 2007, 45(10), 3230–3239.

[19] N.Srivastava, G.Hinton, A.Krizhevsky, " Dropout: a simple way to prevent neural networks from overfitting," Journal of Machine Learning Research 15 (2014), 1929-1958.